

Dense gas in IRAS 20343+4129: an ultracompact HII region caught in the act of creating a cavity

F. Fontani^{1*}, Aina Palau², G. Busquet³, A. Isella⁴, R. Estalella⁵, Á. Sanchez-Monge¹, P. Caselli⁶ and Q. Zhang⁷

¹ INAF-Osservatorio Astrofisico di Arcetri, L.go E. Fermi 5, Firenze, I-50125, Italy

² Institut de Ciències de l'Espai (CSIC-IEEC), Campus UAB-Facultat de Ciències, Torre C5-parell 2, Bellaterra, E-08193, Catalunya, Spain

³ INAF-Istituto di Fisica dello Spazio Interplanetario, Via Fosso del Cavaliere 100, Roma, I-00133, Italy

⁴ Division of Physics, Mathematics and Astronomy, California Institute of Technology, MC 249-17, Pasadena, CA 91125, USA

⁵ Departament de Astronomia i Meteorologia (IEEC-UB), Institut de Ciències del Cosmos, Universitat de Barcelona, Martí Franquès 1, E-08028 Barcelona, Spain

⁶ School of Physics and Astronomy, University of Leeds, Leeds, LS2 9JT, UK

⁷ Harvard-Smithsonian Center for Astrophysics, 60 Garden Street MS78, Cambridge, MA 02138, USA

Accepted date. Received date; in original form date

ABSTRACT

The intermediate- to high-mass star-forming region IRAS 20343+4129 is an excellent laboratory to study the influence of high- and intermediate-mass young stellar objects on nearby starless dense cores, and investigate for possible implications in the clustered star formation process. We present 3 mm observations of continuum and rotational transitions of several molecular species (C_2H , $c-C_3H_2$, N_2H^+ , NH_2D) obtained with the Combined Array for Research in Millimetre-wave Astronomy, as well as 1.3 cm continuum and NH_3 observations carried out with the Very Large Array, to reveal the properties of the dense gas. We confirm undoubtedly previous claims of an expanding cavity created by an ultracompact HII region associated with a young B2 zero-age main sequence (ZAMS) star. The dense gas surrounding the cavity is distributed in a filament that seems squeezed in between the cavity and a collimated outflow associated with an intermediate-mass protostar. We have identified 5 millimeter continuum condensations in the filament. All of them show column densities consistent with potentially being the birthplace of intermediate- to high-mass objects. These cores appear different from those observed in low-mass clustered environments in several observational aspects (kinematics, temperature, chemical gradients), indicating a strong influence of the most massive and evolved members of the protocluster. We suggest a possible scenario in which the B2 ZAMS star driving the cavity has compressed the surrounding gas, perturbed its properties and induced the star formation in its immediate surroundings.

Key words: Stars: formation – ISM: individual objects: IRAS 20343+4129 – ISM: molecules

1 INTRODUCTION

Most of the stars of all masses in the Galaxy form in rich clusters. Despite this, the details of the clustered star formation process are still poorly understood. Studies of *low-mass protoclusters* have started to unveil similarities and differences between isolated and clustered dense cores (e.g. André et al. 2007, Foster et al. 2009, Friesen et al. 2009). Globally

these studies suggest that cluster environment has a relatively smaller influence on the properties of the cores (temperature, mass, velocity dispersion, chemical abundances of early phase molecules) than is typically assumed (Foster et al. 2009). However, the conclusions described above do not include observations of *high-mass star forming regions*. Because the phenomena associated with massive star formation have a stronger impact on the environment (massive outflows, UV radiation, expanding HII regions), it is plausible that these energetic phenomena have major effects on the

* E-mail: fontani@arcetri.astro.it

surrounding dense material. The study of such interaction is especially important to quantify the effect of protostellar feedback on the environment and test recent models of high-mass star formation including outflows and radiation from the newly born stars (e.g. Krumholz et al. 2011, Hennebelle et al. 2011).

Interferometric observations of dense gas and dust tracers (N_2H^+ , mm continuum, NH_3) have revealed the presence of pre-stellar core candidates surrounding ultracompact HII regions (UC HII's) and other massive young stellar objects (YSOs) that do show evidences of such an interaction. For example, Fontani et al. (2009) found that in the protocluster associated with IRAS 05345+3157 the kinematics of two pre-stellar core candidates is influenced by the passage of a massive outflow. UV radiation and powerful outflows affect the chemistry of starless cores in IRAS 20293+3952 (Palau et al. 2007a). On the other hand, a crucial chemical process in pre-stellar cores, i.e. the deuteration of species like N_2H^+ and NH_3 , seems to remain as high as in pre-stellar cores isolated and associated with low-mass star forming regions (Fontani et al. 2008, Busquet et al. 2010, Pillai et al. 2011). Therefore, to date it is not clear if and how the presence of massive objects affects the properties and evolution of the other (pre-)protocluster members.

The protocluster associated with IRAS 20343+4129 (hereafter I20343) represents an excellent laboratory to study this issue. The IRAS source is located to the north-eastern side of the Cygnus OB2 association, at 1.4 kpc of distance from the Sun (Sridharan et al. 2002, Rygl et al. 2011), and two bright nebulous stars, IRS 1 (north) and IRS 3 (south), are found inside the IRAS error ellipse when observed at high angular resolution (Kumar et al. 2002). The bright infrared stars are embedded in a cometary-like cloud whose head, facing the Cygnus OB2 association, is bright at centimeter wavelengths and whose tail, bright in the mid-infrared, is extending for about $10'$ (~ 4 pc) towards the north-east (Fig. 1). This kind of clouds are also known as bright rimmed clouds.

Thanks to interferometric observations of ^{12}CO and 1.3 mm continuum, Palau et al. (2007b) concluded that IRS 1 is an intermediate-mass Class I YSO driving a molecular outflow in the east-west direction, while IRS 3 is likely a more evolved intermediate/high-mass star. This is further confirmed through mid-infrared photometric and spectroscopic observations, from which Campbell et al. (2008) also estimated a bolometric luminosity of the order of $1000 L_\odot$ for both IRS 1 and IRS 3. Furthermore, IRS 3 is at the centre of an UC HII-region detected through VLA centimeter continuum emission (Carral et al. 1999), and of a fan-shaped emission in the $2.12 \mu\text{m}$ rovibrational line of molecular hydrogen (Kumar et al. 2002). East and west of this fan-shaped feature, Palau et al. (2007b) detected molecular gas and dust resolved into several millimeter continuum compact sources. Palau et al. (2007b) interpreted these starless condensations as being accumulated on the walls of the expanding shock front, but could not derive firm conclusions on their origin and nature.

This work aims at better understanding the nature of the dense cores in I20343, and its relation with the neighbouring more evolved objects. To achieve the goal we performed observations of molecular species obtained at high angular resolution with the Combined Array for Research

in Millimeter Astronomy (CARMA) at 3 mm and the Very Large Array (VLA) at 1.3 cm. All selected molecular transitions are commonly used to characterise dense gas: (i) NH_3 and N_2H^+ are excellent tracers of dense and cold cores because either species do not suffer from depletion up to $\sim 10^5 \text{ cm}^{-3}$, and NH_3 is extensively used as thermometer in both low- and high-mass star forming regions; (ii) NH_2D provides an estimate of the degree of deuteration (with NH_3). This combination of diagnostic lines was successfully used by Busquet et al. (2010) to identifying pre-protostellar cores in the proto-cluster associated with IRAS 20293+3952; (iii) C_2H and $c\text{-C}_3\text{H}_2$ are both high-density PDR tracers useful to shed light on the interaction among the cold gas and the UV radiation field coming from IRS 1 and IRS 3. C_2H is also a tracer of cold gas (e.g. Beuther et al. 2008, Padovani et al. 2009). In this paper we concentrate on the gas morphology, temperature and kinematics of the region adjacent to IRS 1 and IRS 3, and confirm the hypothesis proposed by Palau et al. (2007b) that IRS 3 is opening a cavity in the surrounding dense gas and starless material is being accumulated on the cavity walls. In Sect. 2 we describe the observations. The observational results are presented in Sect. 3, and discussed in Sect. 4. In Sect. 5 we summarise the main findings of the work and give a general conclusion.

2 OBSERVATIONS AND DATA REDUCTION

2.1 CARMA

3 mm CARMA observations of I20343 were obtained on 29 Mar 2010 in C- and 01 May 2010 in D-configuration under good weather conditions for observations at 3 mm, characterized by about 5 mm of precipitable water and atmospheric noise rms of about $300 \mu\text{m}$ as measured on a baseline of 100 m at the frequency of 225 GHz. The phase centre was the same as in Palau et al. (2007b), namely: R.A. (J2000) = $20^{\text{h}}36^{\text{m}}07^{\text{s}}.3$ and Dec. (J2000) = $41^\circ39'57''.2$. The local standard of rest velocity of the cloud is assumed to be 11.5 km s^{-1} , as determined from single-dish ammonia observations (Sridharan et al. 2002). The primary beam of the 10 m and 6 m dishes at about 85 GHz is $\sim 73''$ and $121''$, respectively. The single-side-band system temperature during the observations was below 150 K. During C-configuration observations, the correlator provided 4 bands which were configured to observe the continuum, the C_2H , the NH_2D and the N_2H^+ lines simultaneously. D-array observations were obtained with the new CARMA correlator, which provides more bands. Two 500 MHz bands were used to observe the continuum and 5 bands set up to observe the C_2H , N_2H^+ , NH_2D , CCS and $c\text{-C}_3\text{H}_2$ line emission. The pass-band was calibrated by observing 1733-130; flux calibration was set by observing MWC349. The estimated uncertainty of the absolute flux calibration is 10% , and it is determined from periodic observations of MWC349. Atmospheric and instrumental effects were corrected by observing the nearby quasar 2007+404 every 15 minutes.

The tracers observed and the main observational parameters (frequency, synthesised beam, linear resolution, spectral resolution, 1σ rms channel noise, largest detectable angular scale) are reported in Table 1. The CCS line is the only undetected transition and will be not discussed in the

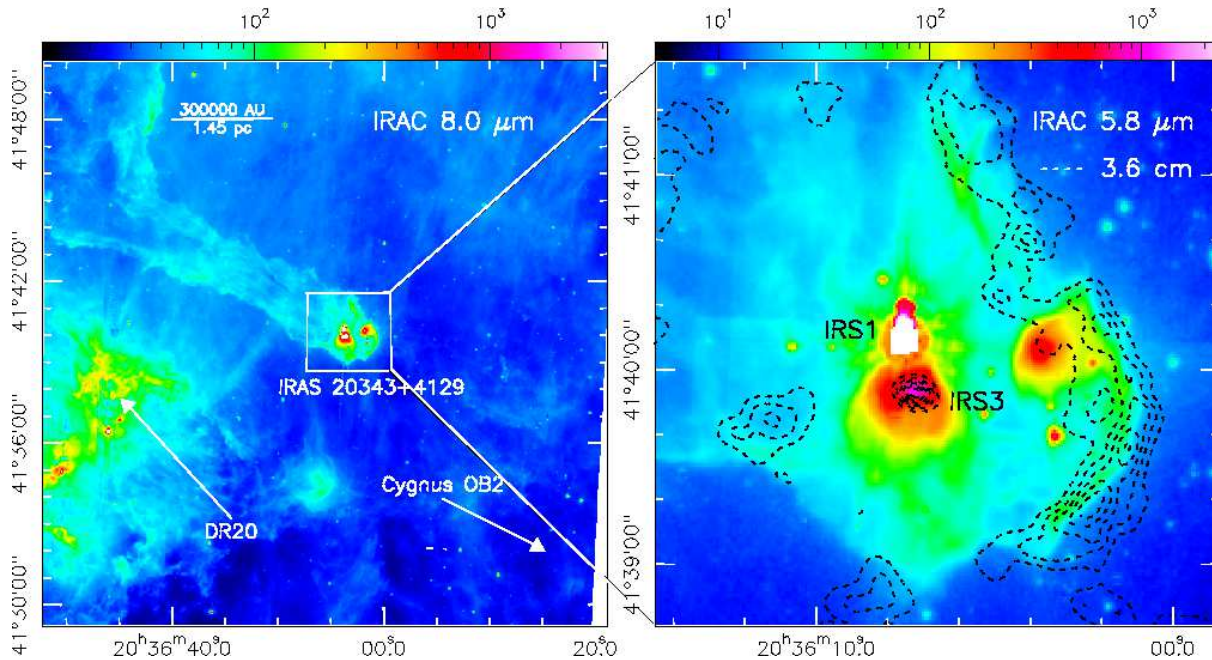


Figure 1. Large-scale view of the surroundings of IRAS 20343+4129 as seen by Spitzer at $8.0 \mu\text{m}$. The Cygnus OB2 association is located to the south-west as shown by the arrow. The enlargement panel to the right shows the region of our interest as it appears in the Spitzer image at $5.8 \mu\text{m}$, where we highlight the two infrared sources IRS 1 (saturated in the IRAC image) and IRS 3. In both panels, the colour scale units are MJy sr^{-1} . The dashed contours correspond to the 3.6 cm continuum emission detected by Carral et al. (1999) with the VLA (D-configuration).

following. The continuum was derived by averaging the 500 MHz bands. Visibility data were edited and calibrated with the MIRIAD package. A minor flagging of the data was performed using the UVFLAG task, mainly to remove the intervals characterized by the bad atmospheric phase coherence. The channel spacing and the corresponding 1σ rms noise are shown in Table 1. Merging the visibilities obtained in C and D configuration, imaging, deconvolution, and analysis of channel maps and continuum were performed using the standard tasks of the GILDAS¹ package (e.g. UVMERGE, UVMAP, CLEAN). Images were created applying natural weighting to the visibilities.

2.2 VLA

I20343 was observed with the Very Large Array (VLA)² at 1.3 and 0.7 cm on 2007 Mar 26 using the array in the D configuration³. The phase center of the observations was R.A. (J2000) = $20^{\text{h}}36^{\text{m}}07^{\text{s}}.51$; Dec. (J2000) = $41^{\circ}40'00''.9$. The data reduction followed the VLA standard guidelines

for calibration of high frequency data, using the NRAO package AIPS. The absolute flux scale was set by observing the quasar 1331+305 (3C286), for which we adopted a flux of 2.52 Jy at 1.3 cm, and 1.45 Jy at 0.7 cm. The quasar 2015+371, with a bootstrapped flux of 1.39 ± 0.02 Jy at 1.3 cm and 2.1 ± 0.2 Jy at 0.7 cm, was observed regularly to calibrate the gains and phases. Final images were produced with the robust parameter of Briggs (1995) set to 5, corresponding to natural weighting. At 7 mm we applied a taper at 60 k λ with the aim of recovering faint extended emission, but no emission was detected at this wavelength.

The VLA was also used to map the $(J,K)=(1,1)$ and $(2,2)$ inversion transitions of the ammonia molecule on 2001 July 23, with the array in the C configuration. The phase center was set to R.A.(J2000) = $20^{\text{h}}36^{\text{m}}08^{\text{s}}.013$; Dec.(J2000) = $+41^{\circ}39'56''.93$. The FWHM of the primary beam at the observed frequency was $\sim 110''$, and the range of projected baselines was 2.59 to 267.20 k λ . The absolute flux calibration was performed by using 3C286, adopting a flux density at 1.3 cm of 2.41 Jy. The phase calibrator was QSO 2013+370, with a 1.3 cm bootstrapped flux density of 2.34 ± 0.04 Jy, and 3C273 was used as the bandpass calibrator. The $\text{NH}_3(1,1)$ and $\text{NH}_3(2,2)$ lines were observed simultaneously in the 4 IF correlator mode of the VLA (with 2 polarizations for each line), providing 63 channels with a spectral resolution of 0.62 km s^{-1} across a bandwidth of 3.13 MHz, plus an additional continuum channel containing the central 75% of the total bandwidth. The bandwidth was centered at the systemic velocity $V_{\text{LSR}}=11.5 \text{ km s}^{-1}$ (Sridharan et al. 2002) for the $\text{NH}_3(1,1)$ line, and at $V_{\text{LSR}}=6.5 \text{ km s}^{-1}$ for the $\text{NH}_3(2,2)$ line (to cover the main and one of the satellite components). Data were

¹ the GILDAS software is developed at the IRAM and the Observatoire de Grenoble, and is available at <http://www.iram.fr/IRAMFR/GILDAS>

² The Very Large Array (VLA) is operated by the National Radio Astronomy Observatory (NRAO), a facility of the National Science Foundation operated under cooperative agreement by Associated Universities, Inc.

³ The VLA continuum observations presented in this work correspond to project AP525. Another project, AP533, was undergone at 3.6, 2 and 0.7 cm, but due to technical problems the data of AP533 project were lost.

Table 1. Observed tracers and basic parameters for the CARMA and VLA observations. The synthesised beam and 1σ rms for CARMA observations are based on the combined configurations C+D (unless when differently specified)

Instrument/Tracer ^a	Frequency ^b (GHz)	Synth. beam ("×")	Linear resolution (pc)	Δv (km s ⁻¹)	1σ rms (Jy beam ⁻¹)	LASC ^c (")
<i>CARMA</i>						
3 mm continuum	86.4197	4.80×4.36	~ 0.03	–	0.0004	33
NH ₂ D $J_{K_a, K_c} = 1_{1,1} - 1_{0,1}$ ($F = 1 - 1$)	85.9263	3.32×2.68	~ 0.02	0.07	0.045 ^d	33
C ₂ H $N_{J, F} = 1_{3/2, 2} - 0_{1/2, 1}$	87.3169	3.35×2.72	~ 0.02	0.41	0.02	33
<i>ortho-c</i> -C ₃ H ₂ $J_{K_a, K_c} = 2_{1, 2} - 1_{0, 1}$ ^e	85.3389	5.81×4.54	~ 0.034	0.07	0.07	33
CCS $N_J = 7_6 - 6_5$	86.1814	5.67×4.84	~ 0.035	0.07	0.04	33
N ₂ H ⁺ $J_{F_1} = 1_2 - 0_1$ ($F = 3 - 2$) ^f	93.1737	2.04×1.94	~ 0.013	0.065	0.07	16
<i>VLA</i>						
7 mm continuum	43.3399	4.67×4.57	~ 0.03	–	0.0004	18
1.3 cm continuum	22.4601	3.02×2.98	~ 0.02	–	0.000057	34
NH ₃ (1,1)	23.6945	4.20×3.19	~ 0.025	0.62	0.0035	34
NH ₃ (2,2)	23.7226	4.25×3.19	~ 0.025	0.62	0.0035	34

^a For the molecular transitions, in the text we will use the following abbreviations: NH₂D ($1_{1,1} - 1_{0,1}$) = NH₂D (1–1); C₂H ($1_{3/2, 2} - 0_{1/2, 1}$) = C₂H (1–0); *c*-C₃H₂ ($2_{1, 2} - 1_{0, 1}$) = *c*-C₃H₂ (2–1); N₂H⁺ ($1_2 - 0_1$) = N₂H⁺ (1–0);

^b rest frequency of the transition listed in Col. 1;

^c largest angular scale (at half power) detectable by the interferometer, estimated from the minimum baseline of the array configuration, and following the appendix in Palau et al. (2010). For the lines observed in C and D configuration, this refers to the merged uv coverage;

^d sensitivity in the merged C+D channel maps smoothed to a spectral resolution of 0.1 km s⁻¹;

^e observed in D configuration only;

^f observed in C configuration only.

calibrated using standard procedures of AIPS, and imaging was performed by applying a taper in the uv -data of 50 k λ and using natural weighting to recover the faint and extended emission. The synthesised beams and rms noises for all the VLA observations are listed in Table 1.

3 RESULTS

3.1 Continuum emission maps

In Fig. 2 the 3 mm (CARMA, C+D configuration, solid contours) and 1.3 cm (VLA, D configuration, dashed contours) continuum emission maps are shown. As reference, we overplot the 1.3 mm continuum emission observed by Palau et al. (2007b, obtained with about a factor 1.5 better angular resolution) as well as the direction of the lobes of the ¹²CO outflow originated by IRS 1 and the (rough) edge of the fan-shaped H₂ emission associated with IRS 3 (Kumar et al. 2002).

The 3 mm continuum emission is resolved into 5 main condensations, which we call MMA, MMB, MMC, MMD and MME in order of increasing R.A. The brightest are MME and MMA, east and west of IRS 3, respectively. From Fig. 2 we note that MME roughly coincides with a 1.3 mm continuum peak (Palau et al. 2007b), while the westernmost one, MMA, encompasses 3 peaks seen at 1.3 mm with SMA. The faintest core, MMC, is detected towards IRS 1. Two more 3 mm condensations, MMD and MMB, are not detected at 1.3 mm. Specifically, MMB is clearly detected close to IRS3, with a shift of only 4'' to the northeast.

The most evident differences among the 3 and 1.3 mm continuum maps are that at 3 mm core MME (MM7 in Palau et al. 2007b) is more extended, and the eastern and western cores are connected by a filamentary emission passing through IRS 3 which is undetected at 1.3 mm. Both differences are probably just the consequence of CARMA being sensitive to larger structures than the SMA. We estimated that the SMA in the observations of Palau et al. (2007b) was sensitive to structures with FWHM < 9'' (using the minimum baseline of the observations and following Palau et al. 2010), while CARMA using C+D configurations was sensitive to structures < 33'' (Table 1), allowing CARMA to recover more extended emission.

As shown in Fig. 2, the continuum emission at 1.3 cm is dominated by one strong and compact source with its emission peak (20^h36^m07.3^s, +41°39'52'') coincident with IRS 3, and matching well the fan-shaped H₂ emission detected by Kumar et al. 2002. A Gaussian fit to this compact centimeter source yields a peak intensity of 0.8 mJy/beam, a flux density of 1.3 mJy, and a deconvolved size of 4.3'' × 1.0'', with PA=78°, corresponding to a size of 6000 AU in the east-west direction (and an unresolved size in the north-south direction). In addition to the compact 1.3 cm source associated with IRS 3, there is a secondary peak at around 6 σ which falls 2'' to the south of MMD, and faint emission joining this secondary peak and the centimeter source in IRS 3, suggesting that the two peaks of centimeter emission could be linked.

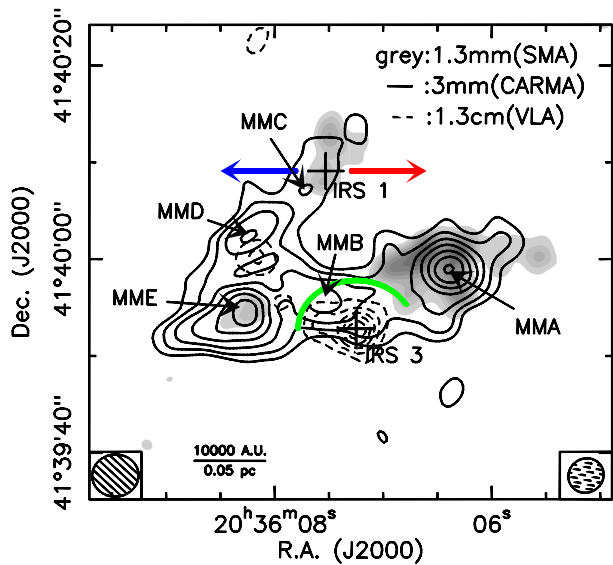


Figure 2. Continuum emission obtained with CARMA at 3 mm (solid contours) and with the VLA at 1.3 cm (dashed contours) towards I20343. The solid contours start from the 3σ rms level (1.2×10^{-3} Jy beam $^{-1}$) and are in steps of 1σ rms. The dashed first contour and step correspond to the 3σ rms level (1.5×10^{-5} Jy beam $^{-1}$) and are in steps of 1σ rms. The grey scale indicates the 1.3 mm continuum emission observed by Palau et al. (2007b) with the SMA (levels = 10% of the maximum, first level = 20% of the maximum). The crosses indicate the two infrared sources identified by Kumar et al. (2002). Red and blue arrows highlight the direction of the blue- and red-shifted emission detected in ^{12}CO (2-1) by Palau et al. 2007b. The green arc roughly shows the fan-shaped feature detected in H_2 μm associated with IRS 3 (Kumar et al. 2002), interpreted as an expanding cavity by Palau et al. 2007b. The ellipse at bottom-left corresponds to the CARMA synthesised beam ($4.8'' \times 4.4''$, at P.A. 92°). The dashed ellipse at bottom-right is the VLA synthesised beam ($3.71'' \times 3.50''$, at P.A. -56.2°).

3.2 Distribution of the Integrated intensity of molecular line emission

3.2.1 Molecular tracers observed with CARMA

The maps of the integrated intensity of the lines observed and detected with CARMA (see Table 1) are shown in Fig. 3. The emission map of each tracer has been superimposed on the images obtained from the Spitzer Space Telescope in the four mid-IR IRAC bands (centred at 3.6, 4.5, 5.8 and $8 \mu\text{m}$, respectively). The location of the near-infrared sources IRS 1 and IRS 3 are also indicated, as well as the direction of the outflow centred on IRS 1 and the edge of the H_2 emission associated with IRS 3, as in Fig. 2. We also superimpose the 1.3 cm continuum emission detected in this work (see Fig. 2), which marks clearly the HII region associated with IRS 3.

The molecular gas seems to be squeezed in between the two dominant mid-IR sources IRS 1 and IRS 3 in all molecules except N_2H^+ . Other compact mid-IR sources are present in the region but do not seem to be associated with any clear molecular counterpart. The diffuse IR nebulosity, especially evident in the 5.8 and $8 \mu\text{m}$ bands, is probably emission from small dust grains distributed around I20343 becoming brighter at longer wavelengths. Some of the dif-

fuse emission detected at $8 \mu\text{m}$ may also be PAHs emission (e.g. Peeters et al. 2002).

The morphology of the integrated intensity of $c\text{-C}_3\text{H}_2$ (2-1) and C_2H (1-0) delineates clearly a cavity around IRS 3 (top panels of Fig. 3), providing a strong support to the hypothesis proposed by Palau et al. (2007b), namely that IRS3 is most likely a more evolved intermediate-mass star creating a cavity. The C_2H emission is more extended than that of $c\text{-C}_3\text{H}_2$, perhaps due to the smaller sensitivity that we have in the $c\text{-C}_3\text{H}_2$ channel maps (see Table 1). Specifically, a narrow filament extended $\sim 30''$ is clearly detected north-east of the field center (Fig. 3, top-left panel), inclined roughly as the tail of the mid-IR cometary shape (see Fig. 1), suggesting that the two features can have the same origin.

The bottom panels in Fig. 3 show the integrated emission of the two Nitrogen-bearing species N_2H^+ and NH_2D . The emission in N_2H^+ consists mainly of one cloud to the east of IRS 3 elongated in the southeast-northwest direction, and extending up to IRS 1, and two smaller clouds, one immediately to the south-west of IRS 3 with no continuum counterpart (called IRS3-SW), and the other associated with MMA. In addition, there is one clump about $1'$ to the west of IRS 3, almost at the border of the bright rim, which falls on a region with no infrared emission associated. On the other hand, the emission of NH_2D consists mainly of one filament elongated in the east-west direction, passing through IRS 3, and with some emission at IRS3-SW. The N_2H^+ clump $1'$ to the west of IRS 3 is detected also in NH_2D , but looks more extended in NH_2D . However, this can be just an effect of the different angular resolution and different filtering of extended emission, as NH_2D was observed with C+D configuration while N_2H^+ was observed in C configuration only (see Table 1).

If we put together the two mostly extended molecular tracers, namely C_2H and NH_2D , we can notice a sort of 'snake-like' filament of molecular gas (Fig. 4) extending from the south-western side of I20343, clearly detected in NH_2D , up to the north-eastern corner, in which a long and narrow filament is detected in C_2H . The bulk of the emission is in between IRS 1 and IRS 3. This 'snake-like' filament matches very well the 1.2 mm continuum emission detected with MAMBO (Beuther et al. 2002, Fig. 4), and its SW-NE inclination follows roughly the 'head-tail' orientation of the mid-IR diffuse cometary emission (Fig. 1), suggesting a possible common origin. However, the highest sensitivity region of the CARMA maps, i.e. the field of view of the 10 m dishes ($\sim 73''$), includes only the central region of the filament (see Fig. 4). For this reason, in this work we focus on the centre of I20343, where the interaction between the two brightest IR sources and the surrounding molecular gas seems predominant, and plan a large interferometric mosaic which will allow us to unveil the overall distribution of the molecular gas and its relation with all the IR sources.

3.2.2 Ammonia (1,1) and (2,2) inversion transitions

The integrated intensity maps of NH_3 (1,1) and (2,2) are presented in Fig. 5. In the (1,1) line, the emission resembles that seen with CARMA in the 3 mm continuum. Four main peaks are detected, which roughly correspond to those detected in the 3 mm continuum. On the other hand, none of the 1.3 mm continuum peaks identified by Palau et al. (2007b)

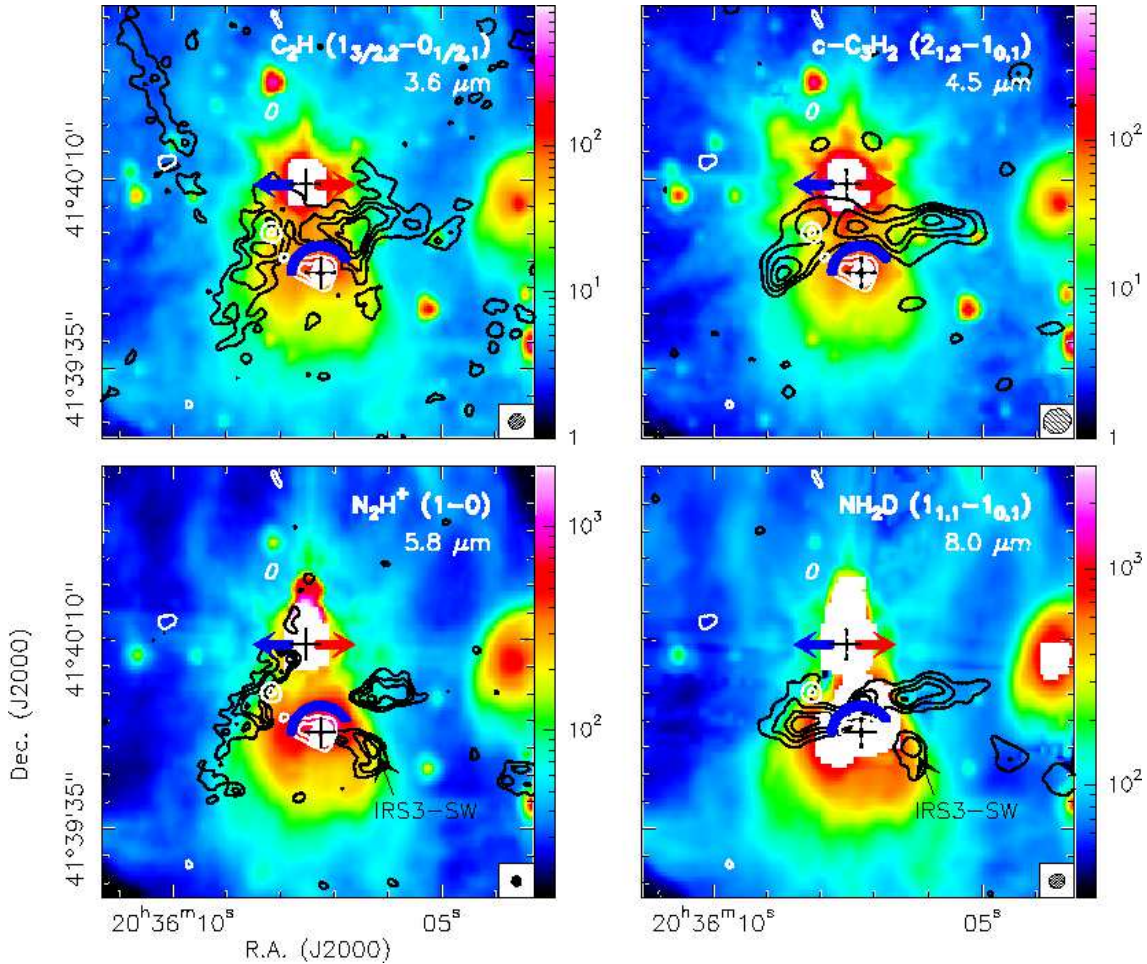


Figure 3. Integrated maps of the molecular lines detected with CARMA (Table 1) towards I20343 and superimposed on the images obtained in the Spitzer-IRAC bands (3.6 μm , 4.5 μm , 5.8 μm , 8 μm , colour scale in MJy sr^{-1} units). In each panel, black contours depict the velocity-averaged emission of the transition labelled at the top-right corner (the corresponding synthesised beam is shown in the bottom-right corner). For all lines, the emission has been averaged over all the velocity channels with signal, except for N_2H^+ (bottom-left panel) for which the integrated emission was averaged over the main group of hyperfine components only. For C_2H and NH_2D , first contour and step correspond to the 20% level of the maximum (corresponding roughly to the 3σ rms level of the averaged map), while for $c\text{-C}_3\text{H}_2$ and N_2H^+ contours start from the 30% level of the maximum and are in steps of 20%. The white contours represent the VLA 1.3 cm (K-band) continuum image (same contours as in Fig. 2). The position of IRS 1 and IRS 3, the associated outflow and fan-shaped H_2 emission are shown as in Fig. 2.

exactly coincides with any of the NH_3 (1,1) peaks, despite the similar angular resolution. The NH_3 (1,1) emission reveals two main clouds, one to the east and the other to the west of IRS 3. The eastern cloud includes MMD and MME and appears elongated in the southeast-northwest direction, similar to the N_2H^+ eastern cloud and to the 3 mm continuum emission. The western cloud has a condensation near MMB (near IRS 3) and another condensation near MMA. The overall emission in the western cloud is elongated in the east-west direction. We stress that NH_3 (1,1) emission is marginally detected also towards IRS 3 and the cavity driven by it, as for the 3 mm continuum. On the other hand, the millimeter continuum sources associated with IRS 1 as well as the ^{12}CO outflow lobes are not detected in ammonia. The NH_3 (2,2) transition is clearly detected towards the eastern side of MME, where 2 peaks are resolved. The NH_3 (2,2) line emission around IRS 3 and towards the west is clumpy, peaking towards MMA and near MMB and IRS3-SW.

From a comparison of the N-bearing to the C-bearing species, both C_2H and $c\text{-C}_3\text{H}_2$ highlight clearly the cavity associated with IRS 3 (see top panels in Fig. 3), while NH_2D and NH_3 trace emission extending east-west passing through IRS 3 (see Fig. 5 and bottom panels of Fig. 3) more similar to that seen in the 3 mm continuum map. Thus, there seems to be a chemical dichotomy in I20343 among Carbon- and Nitrogen-bearing molecules. The exception is represented by N_2H^+ , detected away from IRS 3. This molecule appears to trace the part of the cloud less disrupted by the expanding cavity.

The spectra of the NH_3 (1,1) and NH_3 (2,2) emission, integrated within the 5σ contour polygon of the 3 mm continuum image (except for MMB and MMD, where we used the 3σ contour) are shown in Fig. 6. For IRS3-SW, we used the 5σ rms contour of the NH_2D (1-1) line integrated emission (Fig. 3, bottom-right panel). To compare the different molecular species, in Fig. 6 we also show the integrated spectra of

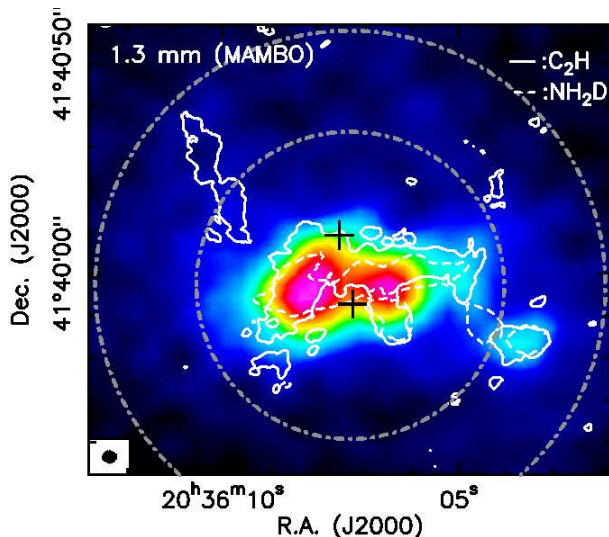


Figure 4. Integrated emission of molecular tracers (white contours) superimposed on the image of I20343 in MAMBO at 1.2 mm (Beuther et al. 2002). The solid white contour depicts the 15% level of the zero-order moment map of C_2H (1–0). The dashed white contour corresponds to the 15% level of the zero-order moment map for the NH_2D (1–1) line. The ellipse in the bottom-left corner shows the CARMA synthesised beam for the C_2H map and it is almost coincident to that of the NH_2D map. The grey dotted-dashed circles represent the primary beams of the CARMA 10 and 6 m dishes (73 and 121 ″), respectively.

NH_2D and N_2H^+ extracted using the same polygons. We do not show the spectra towards MMC because this core is undetected in NH_2D and NH_3 (2,2), and marginally detected in the other lines. Among all the NH_3 (1,1) spectra, MMA shows the strongest emission, and MME shows the broadest lines, of up to 2.2 km s^{-1} . Such a large line broadening in MME could be due to a double velocity component, as suggested by the N_2H^+ spectrum which has 10 times better spectral resolution. Concerning MMB, MMD, and IRS3-SW NH_3 (1,1) spectra, it is striking the anomaly seen in the inner satellite hyperfine lines, with one inner satellite clearly detected above 5σ and the other inner satellite remaining undetected. The anomaly for the non-LTE case due to hyperfine selective photon trapping affects only the outer satellites (red stronger than blue, Stutzki & Winnewisser 1985), allowing us to rule out this possibility in I20343. Rather, anomalies of one inner satellite being stronger than the other have been observed in several works (Lee et al. 2002, Longmore et al. 2007, Purcell et al. 2009) and explained as being due to systematic motions, following the theoretical work of Park (2001). Park (2001) shows that if the core is contracting the inner blue satellite should be stronger than the inner red satellite for a systematic motion in the range of $0.4\text{--}1 \text{ km s}^{-1}$, and for a range of H_2 number densities and NH_3 column densities which are consistent with those derived by us (as we will show in Sect. 3.4). This is the case of MMD and IRS3-SW. On the other hand, if the core is undergoing expanding motions, the prediction is that the inner red satellite should be stronger than the inner blue satellite, as seen for the case of MMB. Thus, it seems that for these three clumps the NH_3 (1,1) anomalous intensity of the hyperfine

components is consistent with contracting/expanding motions.

The MMA NH_3 (1,1) spectrum is a very special case, as the inner satellites are detected at an intensity smaller than that expected for LTE conditions (maximum main-to-satellite ratio in LTE is 3.6, while the ratio for MMA is 4.3). This could be explained if the opacity is high and the excitation temperature for the main line and the satellites is different, with the satellites having a lower excitation temperature (and hence a smaller main beam temperature). A detailed discussion on the temperature ratio between main line and satellites leads to a possible non isothermal core made of two layers, with the external one being hotter than the inner one. If this interpretation is correct, core MMA could be heated externally, perhaps by IRS 3 and/or the infrared sources west of I20343 (see right panel in Fig. 1 and Fig. 3). We give details of this explanation in Appendix A.

We fitted the NH_3 , NH_2D , and N_2H^+ spectra in order to derive the physical parameters of the gas traced by these molecules. To take into account the line hyperfine structure, we followed the method described in the CLASS user manual⁴. The NH_3 (1,1), NH_2D (1–1) and N_2H^+ (1–0) lines were fitted this way, while we fitted the NH_3 (2,2) lines with Gaussians. The derived fit parameters are reported in Table 2, except the line velocities that will be extensively discussed in Sect. 3.3. These parameters have been used to derive the molecular column densities, the derivation of which will be described in Sect. 4.2. To fit the hyperfine structure of MMB, MMD, and IRS3-SW, we used only the detected satellite and the main line, in order to obtain reliable opacities. For NH_3 , in Table 2 we list also the rotation temperature, T_{rot} , obtained from the (2,2)-to-(1,1) intensity ratio following the method outlined in Busquet et al. (2009), which is based on the discussion presented in Ho & Townes (1983). These range from 13 K (in MMD) to 23 K (in IRS3-SW).

In order to obtain a first approach to temperature variations of the dense gas across I20343, we computed the ratio of the integrated NH_3 (2,2)/(1,1), which has been shown to be a reasonable approach to the kinetic temperature (e.g., Torrelles et al. 1993; Zhang et al. 2002). The result is shown in Fig. 7. As can be seen from the figure, the ratio is largest towards three main regions: near IRS 3 (MMB, and IRS 3-SW), to the north of MMA, and to the eastern side of MME. Thus, the spectra toward MMA, which can be explained with external heating, is consistent with the 22/11 ratio map which reveals that the heating comes most likely from the north of MMA. Interestingly, the north of MMA is spatially coinciding with the redshifted CO outflow lobe driven by IRS 1, suggesting that the outflow and the dense gas are interacting (Fig 7). Most intriguing is the high ratio seen at the eastern side of MME, which extends all along the north-south direction and is seen westwards of the H_2 extended emission reported by Kumar et al. (2002). Such a spatial coincidence is suggestive of a possible relation between the high 22/11 ratio and the H_2 emission. Finally, the high 22/11 ratio near IRS 3 could be indicative of direct heating by the UC HII region associated with IRS 3.

⁴ The CLASS program is part of the GILDAS software, developed at the IRAM and the Observatoire de Grenoble, and is available at <http://www.iram.fr/IRAMFR/GILDAS>

Table 2. NH_3 , N_2H^+ , and NH_2D line parameters for the 3 mm continuum cores (except MMC) and the molecular core IRS3-SW. The parameters have been derived from the spectra shown in Fig. 6 using the fitting procedure described in Sect. 3.2.2.

Core	NH_3				N_2H^+			NH_2D		
	T_{ex} (K)	Δv (km s^{-1})	τ^a	T_{rot} (K)	T_{ex} (K)	Δv (km s^{-1})	τ^a	T_{ex} (K)	Δv km s^{-1}	τ^a
MMA	– ^b	1.52	> 1	18(1)	7	1.63	4.6	17	1.05	2.8
MMB	9.7	1.03	3.5	20(7)	–	–	–	20	1.03	2.5
MMD	21.5	1.21	1.4	13(2)	14	0.9	5.2	41	0.89	0.38
MME	19.8	2.2	1.5	18(3)	6	0.7	10	26	1.01	3.2
IRS3-SW	7.9	1.03	3.2	23(7)	13	0.7	3.3	23	0.72	1.8

^a = Total opacity of the line;

^b = in this core the excitation temperature for the main and the satellite lines of the NH_3 (1,1) transition is probably different. See Appendix A for the detailed discussion on the derivation of the physical parameters from NH_3 .

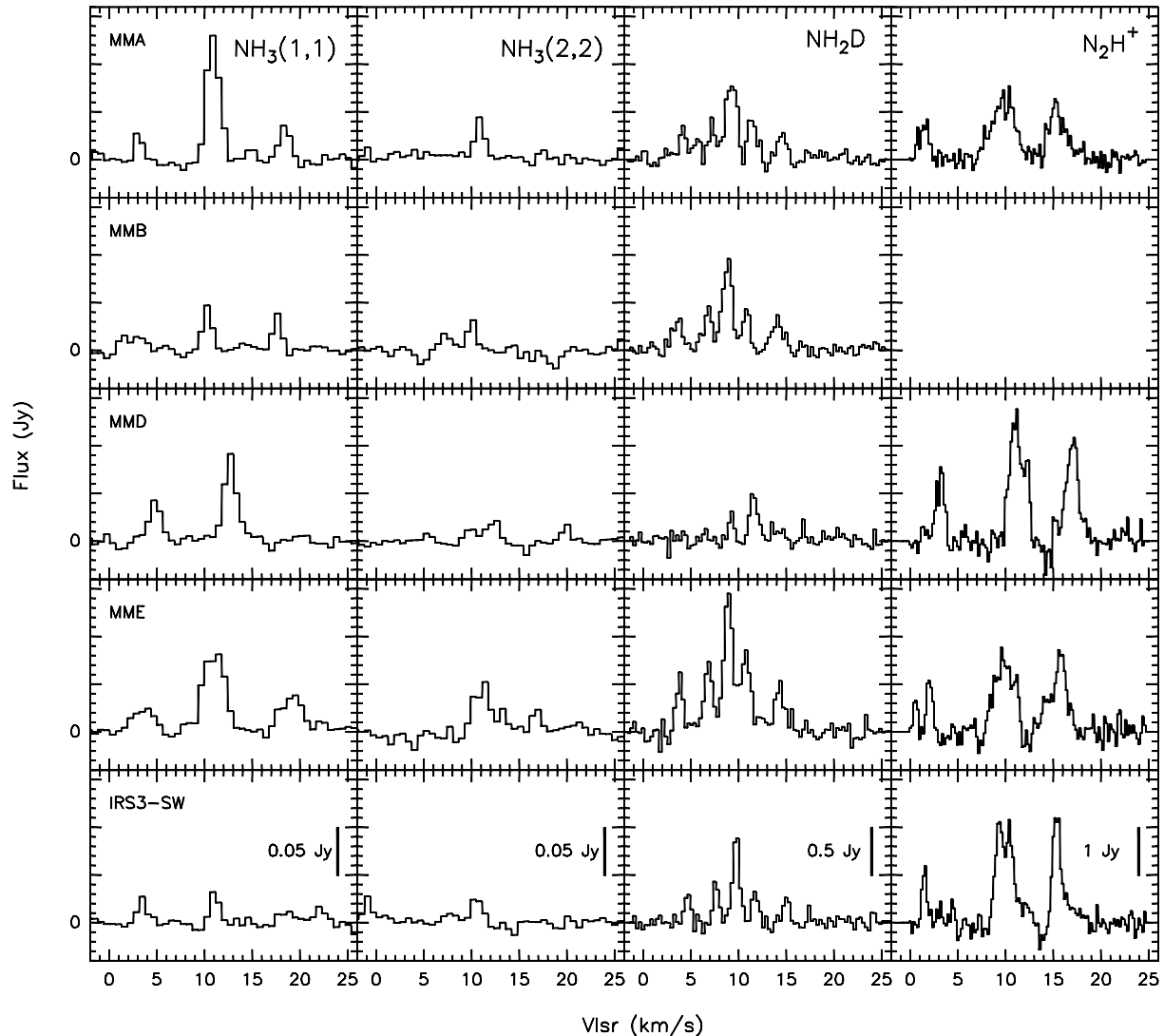


Figure 6. Spectra of the detected transitions of NH_3 , NH_2D and N_2H^+ at the position of the 3 mm continuum condensations (except MMC, undetected in all the lines) and the molecular condensation IRS3-SW. The polygon used to extract the spectra corresponds to: the 5σ rms contour of the 3 mm continuum image for MMA and MME; the 3σ rms contour of the 3 mm continuum image for MMB and MMD; the 5σ rms contour of the integrated emission of NH_2D (1–1) for IRS3-SW.

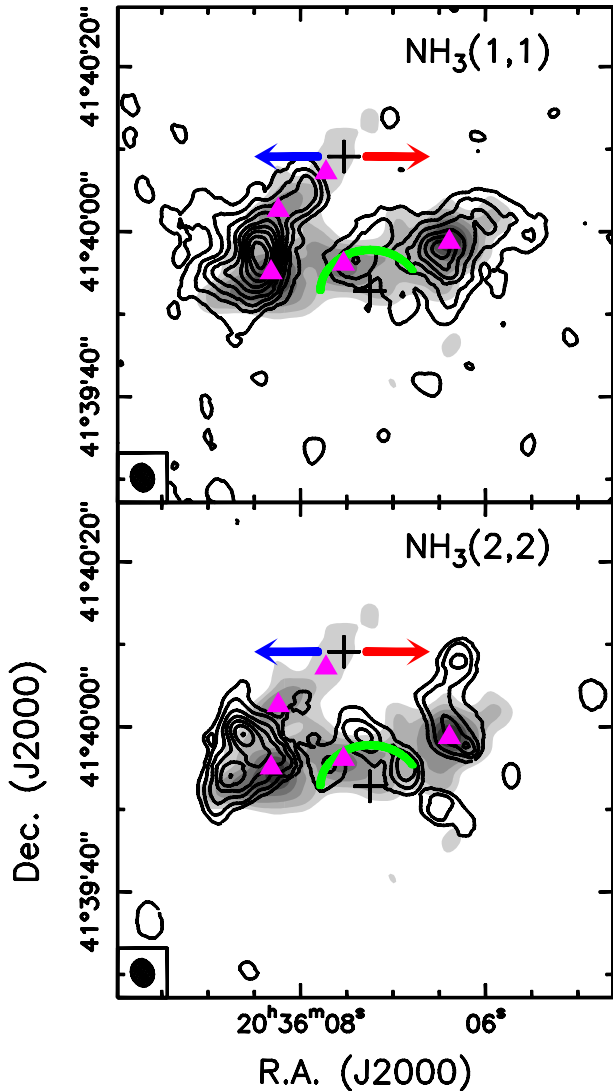


Figure 5. Top panel: integrated emission map of the ammonia (1,1) inversion transition (contours) observed with the VLA towards I20343, superimposed on the 3 mm continuum (CARMA, grey-scale). First contour level and step are the 10% of the peak ($224 \text{ Jy beam}^{-1} \text{ m s}^{-1}$). The ellipse at bottom-left represents the VLA synthesised beam ($4''20 \times 3''19$, at P.A. $\sim 11^\circ$). Purple triangles pinpoint the 3 mm continuum peaks (see Fig. 2). All other symbols (crosses, arrows and semiellipse) are the same as in Fig. 2.

Bottom panel: same as top panel for the (2,2) inversion transition. First contour level and step are the 15% of the peak ($57 \text{ Jy beam}^{-1} \text{ m s}^{-1}$). The synthesised beam in this case is $4''25 \times 3''19$, at P.A. $\sim 13^\circ$.

3.3 Kinematics

To inspect the velocity field, we have extracted from the interferometric channel maps spectra of the molecular transitions detected on grids with regular spacings ($1.5'' \times 1.5''$ for C_2H , $2.5'' \times 2.5''$ for $c\text{-C}_3\text{H}_2$, $1'' \times 1''$ for N_2H^+ , $1.6'' \times 1.5''$ for NH_2D and NH_3). The spectra extracted have been fitted following different methods: for C_2H (1-0), $c\text{-C}_3\text{H}_2$ (2-1) and NH_3 (2,2) we assumed Gaussian lines, while for N_2H^+ (1-0), NH_2D (1-1) and NH_3 (1,1) we fitted the lines

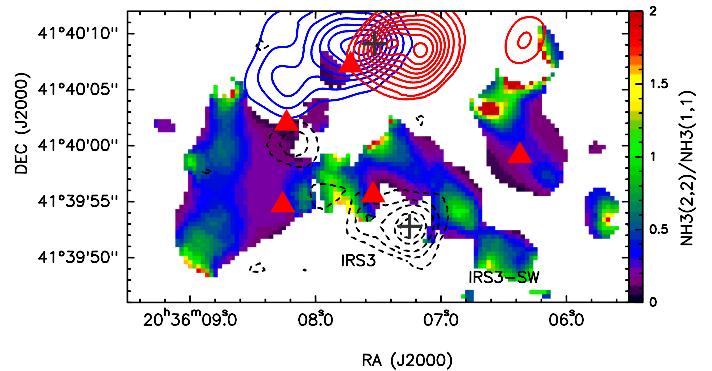


Figure 7. Colorscale: ratio of the integrated NH_3 emission (2,2)/(1,1). Red triangles indicate the 3 mm continuum peaks, which correspond to (from east to west) MME, MMD, MMC, MMB and MMA. The black-dashed contours indicate the VLA 1.3 cm emission (2.5, 5, 7.5, 12, 15 times $50 \mu\text{Jy beam}^{-1}$). The blue/red solid contours depict the high-velocity CO (2-1) blueshifted/redshifted emission (Palau et al. 2007b). Blue contours range from 10 to 99% in steps of 12% of the peak intensity ($21.335 \text{ Jy beam}^{-1} \text{ km s}^{-1}$); red contours are 6, 12 to 99% in steps of 12% of the peak intensity ($41.781 \text{ Jy beam}^{-1} \text{ km s}^{-1}$).

following the method described in Sect. 3.2.2 to take into account their hyperfine structure.

3.3.1 Line peak velocities

Fig. 8 shows maps obtained from the line peak velocities. In all tracers the radial velocities are predominantly blue-shifted to the west and red-shifted to the north-east. The east-west velocity gradient is not uniform and suggests a possible torsion of the gas. Interestingly, the inclination of this gradient with respect to the line of sight is opposite to that of the outflow associated with IRS 1, since the blue lobe of the outflow is located on the side where the dense gas is red-shifted, and vice-versa. In general, all tracers with emission near IRS 3 (in MMB) show that the gas is blueshifted at this position.

3.3.2 Line widths

Maps of the line widths are presented in Fig. 9. The measured line broadenings are generally a factor > 3 higher than the thermal broadening, expected to be of the order of $\sim 0.1 - 0.3 \text{ km s}^{-1}$, indicating that the gas kinematics is largely dominated by non-thermal motions. This finding confirms previous studies in similar intermediate- to high-mass protoclusters (e.g. Palau et al. 2007a, Fontani et al. 2009, Busquet et al. 2010), and represents one of the most important differences between these dense cores and those observed in low-mass star forming regions, where the line widths are dominated by thermal broadening, even in clustered environments (e.g. Kirk et al. 2007, Walsh et al. 2007, Bourke et al. 2011).

In summary we highlight three regions where the gas is more turbulent (Fig. 9): (i) around IRS 3, especially in between IRS 1 and IRS 3 (see the C_2H and $c\text{-C}_3\text{H}_2$ line widths in Fig. 9); (ii) north of MMA, near the red lobe; (iii) towards MMA. The turbulence enhancement around IRS 3 is easily explained by the expanding cavity, while in

MMA and north of it could rather be due to the red-lobe of the outflow. On the other hand, we stress that towards MME and in between IRS 1 and IRS 3 some spectra show a double-velocity component (see e.g. the isolated hyperfine component in the N_2H^+ (1–0) line towards MME in Fig. 6). These are especially evident in the N_2H^+ , NH_3 and NH_2D spectra, but the second component can be seen also in some spectra of C_2H and $c\text{-C}_3\text{H}_2$ close to the cavity. Therefore the large broadening above IRS 3 and in MME could just be due to the superposition of two unresolved velocity components.

Interestingly, for C_2H and N_2H^+ the line broadening is relatively small close to the blue lobe of the outflow associated with IRS 1 and larger besides the red lobe, while the opposite seems to occur for the $c\text{-C}_3\text{H}_2$ (2–1) line (top-middle panel in Fig. 9). This could indicate a selective influence of the flow on the different molecules in the surrounding material. However, we stress that the $c\text{-C}_3\text{H}_2$ emission is very faint at the borders of the region plotted in Fig. 9, where the fit results are affected by large relative errors.

3.3.3 Position-velocity plots

In order to further study the velocity field of the NH_3 emission near IRS 3, we computed position-velocity plots for the NH_3 (1,1) line in the east-west direction, and centred at offset $0''$, $-2''$ with respect to the CARMA phase centre. The final plot is shown in panel "a" of Fig. 10. The NH_3 (1,1) emission in the position-velocity plot shows two main peaks, one corresponding to the eastern cloud and the other corresponding to the western cloud, and both peaks are linked through fainter emission which overall shows a U-like structure. Such a feature resembles the shape predicted by the model of Arce et al. (2011) for an expanding bubble. In this model, an expanding shell would appear as a ring in the (p-v) plots (see their Fig. 5), while we only see the blue-shifted half of it. However, a U-like feature can be explained if the source driving the bubble is slightly displaced (behind the bubble) with respect to the surrounding molecular gas, so that we mainly see the gas which is moving towards us. In fact, the tails of the U-like feature are found, as expected, at approximately the systemic velocity. This suggests that IRS 3 may be pushing the surrounding dense material away (either through its winds/radiation or through the associated HII region), with an expansion velocity (difference between the 'tip' of the U-like feature and the 'tails') of about 2 km s^{-1} (see panel "a" in Fig. 10). A similar expanding shell was recently found around an infrared-source at the centre of a region devoid of gas emission in the intermediate- to high-mass protocluster IRAS 05345+3157 (Fontani et al. 2012).

3.4 Physical parameters from 3 mm and 1.3 cm continuum emission

3.4.1 3 mm

We have identified 5 main condensations in the 3 mm continuum emission map (see Sect. 3.1). Their peak positions are given in Cols. 2 and 3 of Table 3. We also list the angular (θ) and linear (D) diameters (Cols. 6 and 7 in Table 3) computed assuming the sources are Gaussians, and deconvolving the contour at half maximum with a Gaussian beam with HPBW corresponding to the geometric mean of the minor

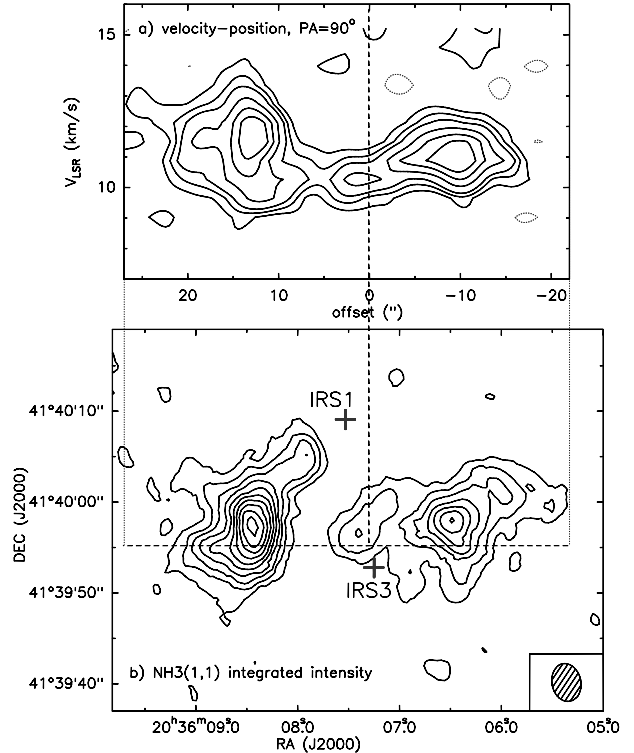


Figure 10. a) NH_3 (1,1) position-velocity plot centred at offset $(0, -2'')$ with respect to the CARMA phase centre and along a cut in the east-west direction. The NH_3 (1,1) data cube was convolved with a beam of $5'' \times 2''$ and $\text{PA}=0^\circ$ to increase signal-to-noise. Contours are: $-3, 3, 6, 9, 15, 21,$ and 27 times $0.001 \text{ Jy beam}^{-1}$. b) NH_3 (1,1) integrated emission map (same contours as in Fig. 5) with the cut of the position-velocity plot of panel "a" indicated by a dashed line. Contours start at 12% of the peak intensity, $224 \text{ Jy beam}^{-1} \text{ m s}^{-1}$, and increase in steps of 10%. The VLA synthesised beam is shown in the bottom-right corner.

and major axes of the CARMA synthesised beam (see Table 1). Because the contours at half maximum were blended, at the edge between two cores we decided to separate the emission arising from the different condensations identifying the peaks and considering the first unblended contour. The same criterion was applied to derive the integrated flux density, F_ν , given in Col. 5 of Table 3.

From F_ν , we have computed the mass of the condensations under the assumptions that the dust millimeter-continuum emission is optically thin, and that the dust temperature equals the gas kinetic temperature. This latter hypothesis implies coupling between gas and dust, which is a reasonable assumption for H_2 volume densities above 10^5 cm^{-3} . Under these assumptions, the gas mass can be derived from the formula:

$$M = \frac{F_\nu d^2}{B_\nu(T)k_\nu}, \quad (1)$$

where d is the source distance, $B_\nu(T)$ is the Planck function at dust temperature T , and k_ν is the dust opacity per unit dust mass. For this latter, we extrapolated the value at 230 GHz given by Kramer et al. (1998), $k_{230} = 0.005 \text{ cm}^2 \text{ g}^{-1}$ (which assumes a gas-to-dust ratio of 100), through the power-law $k_\nu = k_{230}[\nu(\text{GHz})/230]^\beta$. We have assumed $\beta = 2$, which is a typical value derived for dusty envelopes of

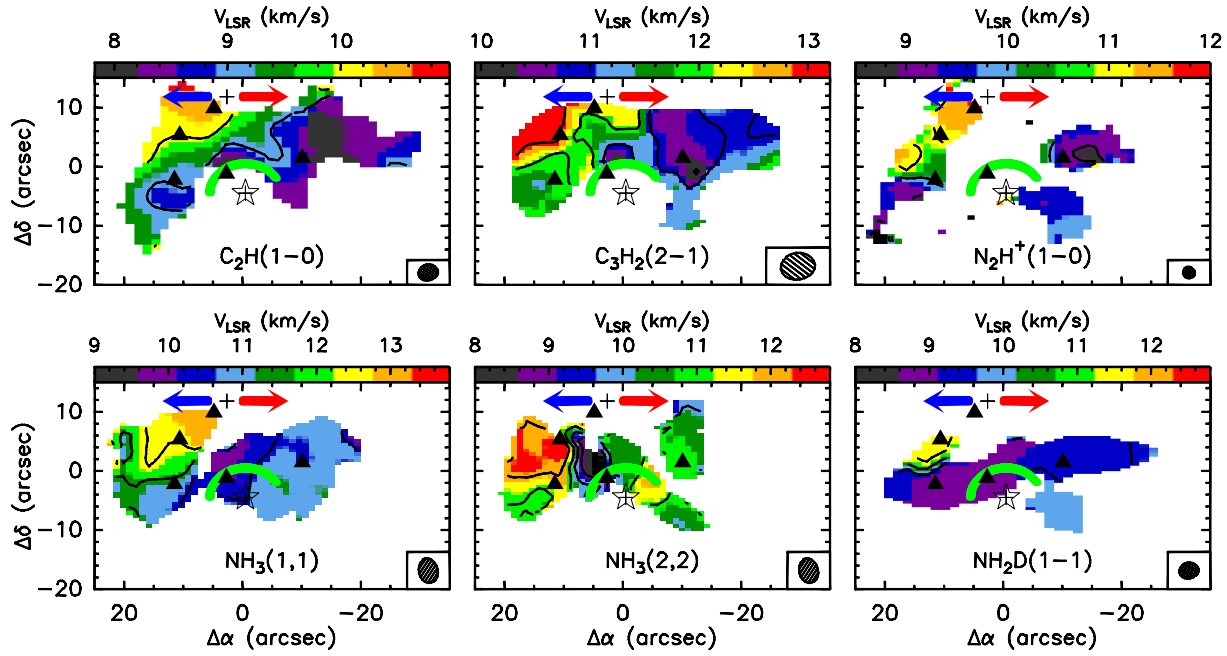


Figure 8. Maps of the line peak velocity for all detected molecular lines. Top panels show (from left to right): $C_2H(1-0)$, $c-C_3H_2(2-1)$ and $N_2H^+(1-0)$. Contours are in steps of 1 km s^{-1} , and range from: 8 to 11 km s^{-1} for C_2H ; 10.5 to 13.5 for $c-C_3H_2$; 9 to 12 km s^{-1} for N_2H^+ . Bottom panels show (from left to right): $NH_3(1,1)$, $NH_3(2,2)$ and $NH_2D(1-1)$. Contours are in steps of 1 km s^{-1} , and range from: 9.5 to 13.5 km s^{-1} for $NH_3(1,1)$; 9 to 13 km s^{-1} for $NH_3(2,2)$; 8.5 to 12.5 km s^{-1} for NH_2D . In each panel, the ellipse in the bottom-right corner represents the CARMA or VLA synthesised beam. The black triangles pinpoint the 3 mm continuum peaks (Sect. 3.1). The position of IRS 1 and IRS 3, as well as the associated outflow and fan-shaped H_2 emission, are depicted in each panel as in Fig. 2.

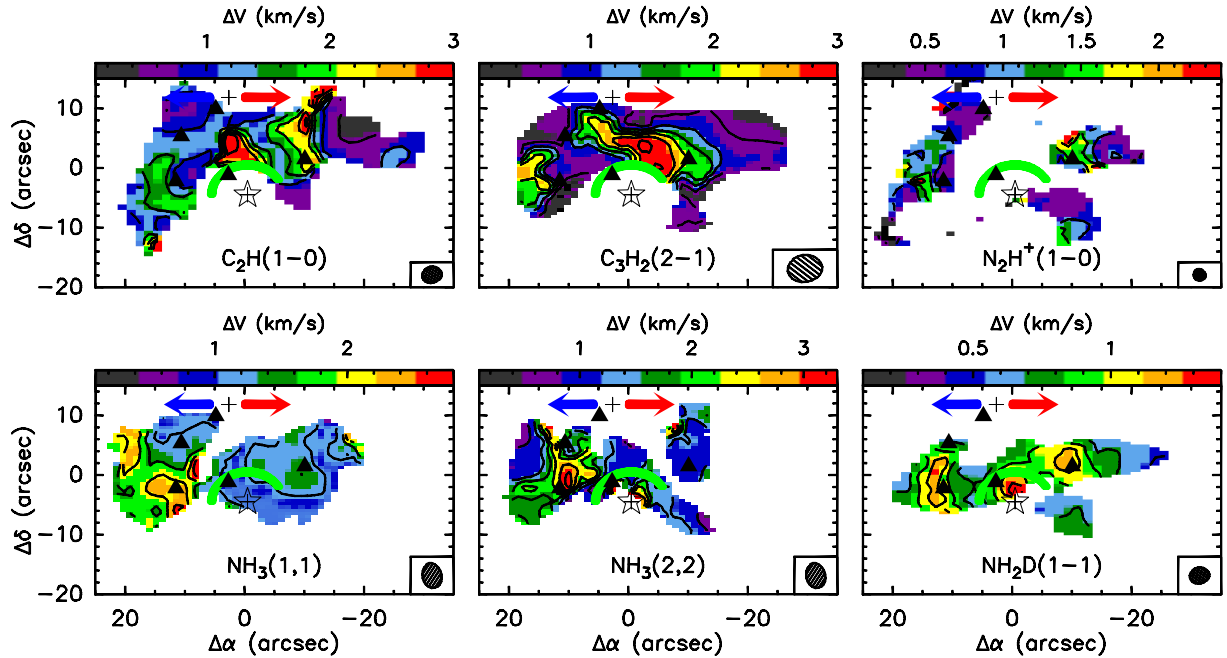


Figure 9. Same as Fig. 8 for the line widths. Contours are in steps of 0.5 km s^{-1} and range from: 0.5 to 3 km s^{-1} for C_2H ; 0.6 to 3.1 km s^{-1} for $c-C_3H_2$; 0.4 to 2.4 km s^{-1} for N_2H^+ ; 0.6 to 2.6 km s^{-1} for $NH_3(1,1)$; 0.8 to 3.2 km s^{-1} for $NH_3(2,2)$; 0.3 to 1.3 km s^{-1} for $NH_2D(1-1)$.

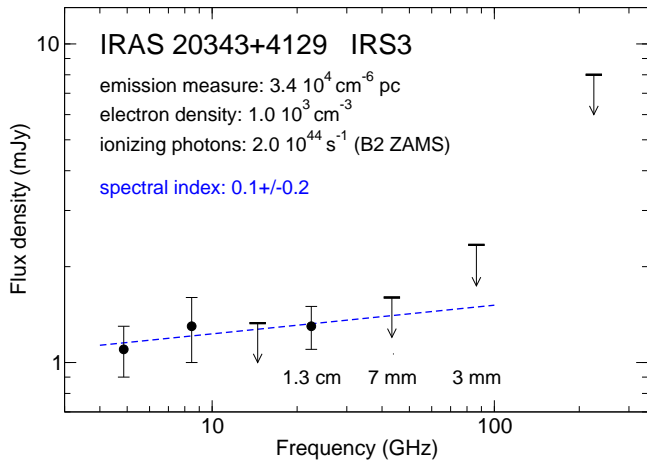


Figure 11. Spectral energy distribution of IRS 3 in the cm/mm range. The physical parameters have been derived assuming the emission at 1.3 cm comes from an optically thin HII region.

massive (proto)stellar objects (e.g. Molinari et al. 2000, Hill et al. 2006). As gas temperature, we have taken the kinetic temperature obtained by extrapolating the rotation temperature derived from the ammonia (2,2)/(1,1) line ratio for each core (see Sect. 3.2.2 and Table 2) following the empirical approximation method described in Tafalla et al. (2004). The kinetic temperatures derived this way are listed in Col. 4 of Table 3, and are in between 14 and 25 K, higher (a factor 1.5 – 2) than the values measured typically in low-mass clustered starless cores (e.g. André et al. 2007, Foster et al. 2009) which are around 10–13 K. For MMC, undetected in NH₃ (2,2), we decided to give a range of masses computed in the temperature interval 15–30 K.

The resulting masses are listed in Col. 8 of Table 3. All fragments have masses consistent with intermediate-to high-mass embedded objects. The most massive one is MME (23 M_⊙). By assuming spherical and homogeneous cores, we have derived the average H₂ volume and column densities. The average volume and column densities (given in Cols. 9 and 10 of Table 3) are of the order of 10^{6–7} cm^{–3} and 10^{23–24} cm^{–2}. Such high column densities are consistent with being the birthplaces of intermediate- and/or high-mass objects (e.g. Krumholz & McKee 2008).

3.4.2 1.3 cm

In Sect. 3.1 we showed that the centimeter emission is dominated by one single source associated with IRS 3 and extending towards the east. In addition, a secondary source near MMD was also identified. A 3.6 and 6 cm source associated with IRS 3 is already reported by Miralles et al. (1994) and Carral et al. (1999). However, from these two measurements only, and taking into account the uncertainties, the spectral index of the centimeter source associated with IRS 3 could not be well determined (e.g., Palau et al. 2007b). Our new measurement at 1.3 cm allows to better constrain the spectral index of the source to 0.1 ± 0.2 (Fig. 11). Such a spectral

index is consistent with optically thin free-free emission favoring the interpretation that the centimetre emission comes from an HII region rather than a thermal radio jet (which typically have steeper spectral indices). We calculated the physical parameters of the ionised region at 1.3 cm assuming the emission is optically thin, and obtained an emission measure of $3.4 \times 10^4 \text{ cm}^{-6} \text{ pc}$, characteristic of UC HII regions, and a flux of ionising photons of $2 \times 10^{44} \text{ s}^{-1}$, consistent with the HII region being ionised by an early-type B2 star (Panagia 1973). Interestingly, the extension of such an UC HII region towards the east is similar (although larger in size) to the extension seen in [NeII] emission by Campbell et al. (2008), and which is interpreted as due to the expansion of the ionised gas and disruption of the natal envelope. In this context, the secondary centimetre peak near MMD could be related as well to the expanding ionised gas. We estimated the possible contribution of free-free emission to the flux measured at 3 mm for MMB, and is of $\sim 0.3 \text{ mJy}$ (4σ of 1.3 cm observations, and using the spectral index of 0.1), out of 4.6 mJy, or 6%. Thus, thermal dust emission is the main contribution to the 3 mm continuum emission in MMB. Finally, we estimated an upper limit for the 3 mm emission associated with IRS 3 of 2.3 mJy, measured as the 3 mm flux density inside the 4σ contour of the centimeter emission (Fig. 11), and we cannot rule out the possibility of the UC HII region being still associated with remnant natal dust, although a projection effect could be also possible.

4 DISCUSSION

4.1 Column densities of the PDR tracers C₂H and *c*-C₃H₂

The two carbon-bearing species C₂H and *c*-C₃H₂ are among the most abundant simple carbon-chain molecules detected in the interstellar medium, and are believed to be good tracers of PDRs (Lucas & Liszt 2000, Pety et al. 2005, Gerin et al. 2011). C₂H is formed either from photodissociation of acetylene (C₂H₂) followed by dissociative recombination of C₂H₂⁺ (Mul & McGowan 1980) or through neutral-neutral reaction between C and CH₂ in hot gas (Sakai et al. 2010). *c*-C₃H₂ is believed to be formed by dissociative recombination of *c*-C₃H₃⁺. Both species benefit from the presence of atomic carbon not locked in CO, and a good correlation between the two tracers has been found at the illuminated surface of the Horsehead nebula (Pety et al. 2005, Gerin et al. 2009), as well as in both diffuse and translucent clouds (Lucas & Liszt 2000, Gerin et al. 2011).

We have investigated the relation among the two species in I20343. For this purpose, we have extracted the spectra of C₂H (1–0) and *c*-C₃H₂ (2–1) on a grid of spacing 2.5'' × 2.5'' (roughly half of the CARMA synthesised beam at the frequency of the *c*-C₃H₂ (2–1) transition), and fitted the spectra with Gaussian lines. Then, from the integrated intensity obtained from the fits, we have computed the column densities assuming that both lines are optically thin. This assumption is mandatory because the opacity of the lines cannot be directly measured (for the C₂H (1–0) line we observed only the main hyperfine component, and we do not have isotopologues for *c*-C₃H₂). However, given that the line profiles generally do not show effects due to high optical

Table 3. Peak position, angular and linear diameter, integrated flux density, mass, H₂ volume and column density of the 3 millimeter condensations detected with CARMA. The masses are computed for $\beta = 2$, and assuming the temperatures derived from ammonia. The H₂ volume and column densities are calculated assuming a spherical source with diameter equal to the deconvolved level at half maximum. F_ν has been obtained by integrating the continuum flux density inside the 3 σ contour level.

Core	Peak position		T_k^a (K)	F_ν (mJy)	Diameter		M_{cont} (M_\odot)	n_{H_2} ($\times 10^6 \text{ cm}^{-3}$)	$N(\text{H}_2)$ ($\times 10^{23} \text{ cm}^{-2}$)
	R.A.(J2000)	Dec.(J2000)			θ_s ($''$)	D (pc)			
	20 ^h 36 ^m								
MMA	06 ^s .37	+41°39'59''1	22 ^b	7.4	7.3	0.049	21	6.7	10.3
MMB	07 ^s .54	+41°39'55''6	25	4.6	6.8	0.046	11	4.5	6.4
MMC	07 ^s .72	+41°40'07''2	–	1.9	5.5	0.037	8 ^c ,4 ^d	6.2 ^c ,2.9 ^d	7.1 ^c ,3.3 ^d
MMD	08 ^s .23	+41°40'02''0	14	3.7	6.3	0.043	17	8.7	11.4
MME	08 ^s .26	+41°39'54''7	22	8.3	8.0	0.054	23	5.7	9.6

^a = Derived from T_{rot} as explained in Sect. 3.4;

^b = see Appendix A for the derivation of T_k from ammonia for this core;

^c = assuming a temperature of 15 K;

^d = assuming a temperature of 30 K.

depths, we are confident that the assumption is reasonable. We used the general formula for optically thin transitions (compare to, e.g., Eq. A.3 in Pillai et al. 2007):

$$N_{\text{tot}} = \frac{3h}{8\pi^3} \frac{Q(T_{\text{ex}})}{S\mu^2} \frac{W}{J_\nu(T_{\text{ex}}) - J_\nu(T_{\text{BG}})} \frac{e^{\left(\frac{E_J}{kT_{\text{ex}}}\right)}}{e^{h\nu/kT_{\text{ex}}} - 1} \quad (2)$$

where: E_J and S are energy of the upper level and line strength, respectively, W is the integrated intensity of the line, $Q(T_{\text{ex}})$ is the partition function at the temperature T_{ex} , ν the line rest frequency, $J_\nu(T_{\text{ex}})$ and $J_\nu(T_{\text{BG}})$ are the equivalent Rayleigh-Jeans temperature at frequency ν computed for the excitation and background temperature ($T_{\text{BG}} \sim 2.7 \text{ K}$), respectively; μ the molecule's dipole moment (0.77 Debye for C₂H and 3.27 Debye for *c*-C₃H₂). For C₂H, in Eq. (2) W has been obtained by multiplying the integrated emission of the hyperfine component observed for its relative intensity (0.416). As excitation temperature, we have assumed a reasonable value of 20 K based on the excitation temperatures computed for the other lines (see Table 2). The values of E_J , $S\mu^2$ and Q have been taken from the Cologne Database for Molecular Spectroscopy (CDMS⁵, Müller et al. 2001). For this latter, we have extrapolated the values tabulated to an excitation temperature of 20 K. For *c*-C₃H₂, the *ortho*-/*para*- ratio is included in the partition function.

The results are shown in Fig. 12. The column density of C₂H is of the order of 10^{14} cm^{-2} across the cloud (Fig. 12, top panel), while that of *c*-C₃H₂ is of the order of 10^{12} cm^{-2} (Fig. 12, middle panel). The C₂H column densities are generally larger than those found by Gerin et al. (2011), who measured column densities of 10^{13} cm^{-2} , while those of *c*-C₃H₂ are more consistent. Their ratio is on average of the order of 200 - 400 (Fig. 12, bottom panel), i.e. one order of magnitude larger than the value 20 - 30 measured in translucent clouds (Gerin et al. 2011), as well as in diffuse high latitude clouds (Lucas & Liszt 2000) and in the Horsehead nebula (Pety et al. 2005). On the other hand, the chemical models of PDRs in Gerin et al. (2011) seem to be more consistent with our observational results rather than with theirs, be-

cause the models predict total column densities consistent with our values for both species, and ratios of the order of 100 or even more (see their Table 5). Interestingly, we find the largest ratios (around 400–800) close to the outflow lobes and to the east and west of the cavity walls, where the gas is probably less dense because most disrupted. Significant enhancement can be noticed also in the eastern clump, in between MMD and MME, where 1.3 cm emission is detected (see Sect. 3.1 and Fig. 2). This would confirm strongly that both molecules are produced in PDR regions, and that they are maybe tracing a low density envelope in which the dense cores detected in N₂H⁺ and NH₃ are embedded.

4.2 Chemical differentiation and nature of the 3 mm continuum cores

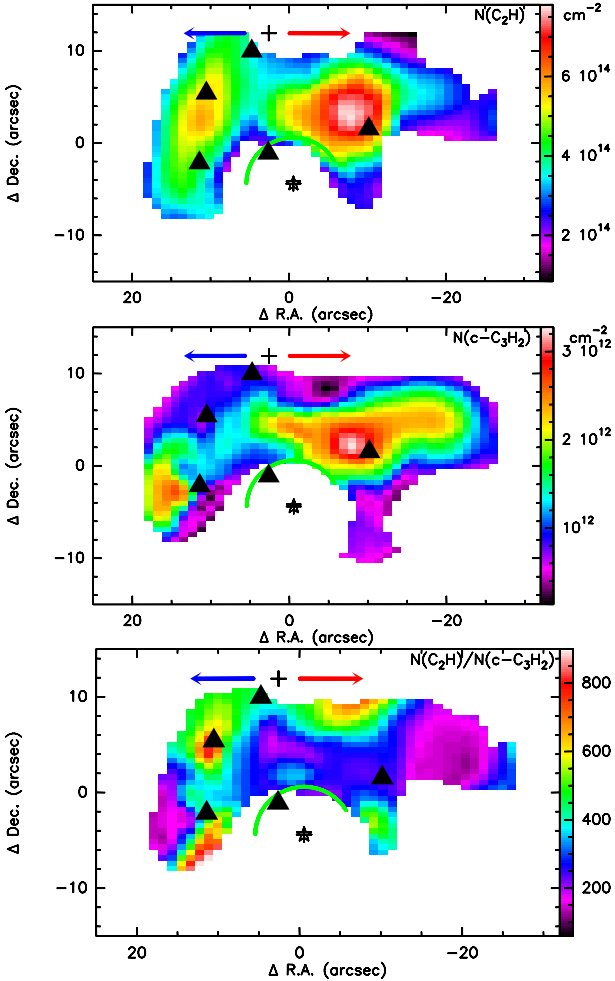
Studies of intermediate- and high-mass star-forming regions suggest that the relative abundance ratio NH₃-to-N₂H⁺ is an evolutionary indicator for dense cores (e.g. Palau et al. 2007a, Fontani et al. 2012): cores with no signs of star formation typically have larger NH₃-to-N₂H⁺ column density ratio than cores associated with active star formation. Also, Fontani et al. (2008) and Busquet et al. (2010) have measured that the deuterated fraction (i.e. the column density ratio of a deuterated species to that of the hydrogenated counterpart) of NH₃ and N₂H⁺ is of the order of 0.1 in pre-protostellar core candidates, as high as in low-mass pre-stellar cores, while it is lower in more evolved objects. With this in mind, we have investigated the evolutionary stage of the millimeter cores in I20343 based on the column density ratios NH₃-to-N₂H⁺ and NH₂D-to-NH₃. From the line parameters derived in Sect. 3.2.2 (see Table 2) we have computed the total column densities of NH₃, NH₂D and N₂H⁺ from Eq. (A1) of Caselli et al. (2002) because all lines are optically thick (except NH₂D (1–1) in MMD, but the opacity is well-constrained). As for the other parameters, for a detailed discussion on the NH₃ data of MMA see the Appendix A.

In Table 4 we report the column densities of NH₃, NH₂D and N₂H⁺, and the column density ratios NH₂D-to-NH₃ and NH₃-to-N₂H⁺. The NH₂D-to-NH₃ ratio is of order 0.1 (from ~ 0.07 to 0.15), and does not change greatly from

⁵ <http://www.astro.uni-koeln.de/cdms/>

Table 4. Total column densities of NH_3 , NH_2D and N_2H^+ for the 3 mm continuum cores, except MMC, and the additional core IRS3-SW.

core	$N(\text{NH}_3)$ ($\times 10^{15} \text{ cm}^{-2}$)	$N(\text{N}_2\text{H}^+)$ ($\times 10^{13} \text{ cm}^{-2}$)	$N(\text{NH}_2\text{D})$ ($\times 10^{14} \text{ cm}^{-2}$)	$N(\text{NH}_2\text{D})\text{-to-}N(\text{NH}_3)$	$N(\text{NH}_3)\text{-to-}N(\text{N}_2\text{H}^+)$
MMA	$> 2.41^6$	7(2)	2.2(0.2)	< 0.09	> 34
MMB	2.3(0.6)	–	2.6(0.3)	0.11(0.04)	–
MMD	3.1(0.7)	13(4)	2.1(0.2)	0.068(0.002)	24(13)
MME	4.4(0.7)	5.5(0.7)	6.8(0.7)	0.15(0.04)	80(23)
IRS3-SW	1.8(0.4)	6(3)	2.1(0.2)	0.12(0.04)	30(22)

**Figure 12.** From top to bottom: Column density map of C_2H and $c\text{-C}_3\text{H}_2$, and their ratio, derived from the CARMA observations. For the column density derivation of both species, an excitation temperature of 20 K has been adopted. The other symbols are the same as in Figs. 8 and Fig. 9.

core to core. Such values are much larger than the cosmic D/H ratio, estimated to be $\sim 10^{-5}$ (Linsky et al. 2006), and comparable to those measured towards low-mass pre-stellar cores (Roueff et al. 2005) and infrared dark clouds (Pillai et al. 2007). This implies that the deuteration in the cores of I20343 is as high as in colder and more quiescent environments, despite the relatively higher gas temperature and turbulence, and confirms previous findings in other dense cores

associated with intermediate- to high-mass star-forming regions (e.g. Busquet et al. 2010, Pillai et al. 2011). Interestingly, relatively high values are found also close to the UC HII region associated with IRS 3, in MMB and IRS3-SW. Because NH_2D is efficiently formed on dust grains, a strong UV radiation can heat the dust and cause NH_2D evaporation thus increasing its abundance. On the other hand, a strong UV radiation could (at least partly) decrease the abundance of NH_3 , due to its interaction with H^+ to form NH_3^+ (e.g. Fuente et al. 1993).

Concerning the $\text{NH}_3\text{-to-}N_2\text{H}^+$ ratio, we find the largest value in MME (~ 80). The enhancement of the $\text{NH}_3\text{-to-}N_2\text{H}^+$ ratio can be understood when freeze-out of species heavier than He becomes important (see e.g. Flower et al. 2006), so that it is expected to increase when the starless core gets closer to the onset of star formation. In this scenario, the fact that MME has the largest $\text{NH}_3\text{-to-}N_2\text{H}^+$ ratio suggests that this core could be close to the onset of gravitational collapse, i.e. MME could be a candidate massive pre-stellar core. However, Palau et al. (2007b) measured with the SMA a mass of only $0.7 M_\odot$ from the 1.3 mm continuum, while we find $23 M_\odot$. This discrepancy likely comes from extended flux filtered out by the SMA, which means that the core is quite flat and not centrally-peaked as expected for a pre-stellar core.

Based on the results of this work, we propose our final interpretation for the nature of each one of the 3 mm condensations:

- MMA is probably a protostar candidate. Although it does not show any embedded infrared source, its relatively high T_{rot} , large line broadening, and $\text{NH}_2\text{D-to-NH}_3$ lower than in other cores suggest that this condensation is evolved.

- MME is likely a pre-stellar core, because it shows high $\text{NH}_2\text{D-to-NH}_3$ and $\text{NH}_3\text{-to-}N_2\text{H}^+$ ratios, is more quiescent than MMA and it does not appear fragmented into smaller condensations when observed at higher angular resolution (Palau et al. 2007b). Assuming a typical star formation efficiency of $\sim 30\%$, the core, the mass of which is $23 M_\odot$, has the potential to form an intermediate- to high-mass object.

- the nature of MMB, MMC and MMD is less clear. Due to the low $\text{NH}_2\text{D-to-NH}_3$ and $\text{NH}_3\text{-to-}N_2\text{H}^+$ ratios, MMD could be a protostellar object, consistent with clear hints of contraction motions seen in the NH_3 (1,1) spectrum, while for MMB we found hints of expansion due to asymmetric emission in the two inner satellites (see Sect. 3.2.2). Certainly, all condensations are perturbed (MMB by the ionisation front from IRS 3, MMC by IRS 1 and the outflow associated with it, MMD perhaps by a combination of both).

Only higher sensitivity and angular resolution observations will allow to better understand the nature of these cores.

4.3 Interaction of IRS 1 and IRS 3 with the dense gas: an expanding cavity

The most striking result of this work is the clear confirmation of a cavity opened by IRS 3 in the molecular surrounding gas, and a tight interaction between this cavity and the surrounding dense gas. We have found several evidences of this: (i) the morphology of all the molecular tracers, especially in C_2H and $c-C_3H_2$, delineates a cavity around IRS 3 and the 1.3 cm continuum map resolving the ionised gas perfectly matches the profile of the cavity; (ii) the NH_3 integrated intensity (2,2)/(1,1) ratios are large near IRS 3; (iii) the line widths are also large near IRS 3, specially in C_2H and $c-C_3H_2$; (iv) the position-velocity plot of NH_3 shows a U-structure typical of an expanding shell; (v) in the MMB core we found hints of expansion in the NH_3 (1,1) spectrum due to different intensity of the two inner satellites. These evidences of such an interaction are shown for the first time in this work.

If we put together all the results obtained, we speculate about a possible scenario that describes the star formation history in I20343: IRS 1 and IRS 3, both having bolometric luminosities of about $1000 L_\odot$, seem to come from the same natal cloud while being clearly in different evolutionary stages, which points towards different generations of (intermediate- to high-mass) star formation in I20343. In this context, IRS 3 could have induced the formation of IRS 1, as could be inducing star formation on the west (in MMA). On the other hand, in this bright-rimmed cloud the star formation probably has not been triggered by the UV radiation from the Cygnus OB2 association stars, because IRS 3, the massive star that formed first, is relatively distant from the bright rim, and the dense gas where we find the bulk of the current star formation activity is around IRS 3 and away from the bright rim. Therefore, the star formation seems to be dominated by IRS 3, which has been caught in the act of pushing away and disrupting its natal cloud.

5 SUMMARY AND CONCLUSIONS

The protocluster associated with the centre of I20343 is an excellent location where the interaction between evolved intermediate- and high-mass protostellar objects and dense (starless) cores can be studied. We have derived the physical and chemical properties of the dense gas by means of CARMA and VLA observations of the millimeter and centimeter continuum, and of several molecular tracers (C_2H , $c-C_3H_2$, NH_3 , NH_2D , N_2H^+). Below, we summarise the main results.

- Morphologically, the dense gas is distributed in a filament oriented east-west that passes in between IRS 1 and IRS 3, the two most massive and evolved objects. We resolve the dense gas into five millimeter continuum condensations. All of them show column densities consistent with potentially being the birthplace of intermediate- to high-mass objects, although the masses derived from continuum suggest that they can form intermediate-mass objects more likely.

- We confirm the presence of an expanding cavity driven by IRS 3 demonstrated mainly by the shape of the emission in the two PDR tracers C_2H and $c-C_3H_2$, as well as by hints of expanding motions from both the position-velocity diagrams and the asymmetric intensity of the two inner satellites of the NH_3 (1,1) line of the millimetre core closest to IRS 3 (MMB).

- The non-thermal line widths across the filament indicate that the gas kinematics is dominated by turbulence, similarly to other intermediate- and high-mass star-forming regions and different from low-mass dense starless cores.

- The rotation and kinetic temperatures derived from ammonia are on average larger than those typically found in cores associated with low-mass star-forming regions, especially around the cavity walls. The most massive and extended millimeter core, MME, shows physical and chemical signatures of an intermediate- to high-mass pre-stellar core candidate.

- We have better constrained the spectral index of the radio-continuum emission associated with IRS 3, which turns out to be flat, and thus the ionised gas comes from a region photoionised by the B2 ZAMS star at the centre of IRS 3.

- the column density ratio $C_2H/c-C_3H_2$ is of the order of 200-400 across the source and is higher where the dense gas is getting disrupted.

- the deuterated fraction NH_2D -to- NH_3 is of the order of 0.1 in all cores, as large as in low-mass pre-stellar cores and infrared dark clouds. We find high levels of deuteration also close to the cavity driven by IRS 3. We speculate that evaporation of NH_2D and NH_3 destruction caused by the UV radiation field can influence this high deuteration.

These findings undoubtedly confirm a tight interaction in I20343 between the most massive and evolved objects and the dense surrounding starless cores in several respects (kinematics, temperature, chemical gradients), and suggest that IRS 3 could have induced the formation of IRS 1 and of the other gaseous condensations accumulated on the cavity walls. However, the large-scale morphology of the molecular tracers suggests that we are likely seeing only a limited portion of a very extended gaseous filament. Only a large pc-scale mosaic will allow us to fully trace the distribution of the dense gas in the region and delineate a complete view of the core population.

ACKNOWLEDGMENTS

Support for CARMA construction was derived from the Gordon and Betty Moore Foundation, the Kenneth T. and Eileen L. Norris Foundation, the James S. McDonnell Foundation, the Associates of the California Institute of Technology, the University of Chicago, the states of California, Illinois, and Maryland, and the National Science Foundation. Ongoing CARMA development and operations are supported by the National Science Foundation under a cooperative agreement, and by the CARMA partner universities. We acknowledge support from the Owens Valley Radio Observatory, which is supported by the National Science Foundation through grant AST 05-40399. AP is grateful to Inma Sepúlveda for insightful discussions. AP is supported by the Spanish MICINN grant AYA2008-06189-C03 (co-funded

with FEDER funds) and by a JAE-Doc CSIC fellowship co-funded with the European Social Fund under the program ‘Junta para la Ampliación de Estudios’. GB is funded by an Italian Space Agency (ASI) fellowship under contract number I/005/07/01. We are grateful to the anonymous referee for his/her valuable comments and suggestions.

REFERENCES

- André, Ph., Belloche, A., Motte, F., Peretto, N. 2007, *A&A*, 472, 519
- Arce, H.G., Borkin, M.A., Goodman, A.A., Pineda, J.E., Beaumont, C.N. 2011, *ApJ*, 742, 105
- Beuther, H., Semenov, D., Henning, Th., Linz, H. 2008, *ApJ*, 675, L33
- Beuther, H., Schilke, P., Menten, K.M. et al. 2002, *ApJ*, 566, 945
- Bourke, T.L., Myers, P.C., Caselli, P. et al. 2011, arXiv:1111.4424
- Briggs, D.S. 1995, 187th American Astronomical Society Meeting, Vol. 27, p.1444
- Busquet, G., Palau, Aina, Estalella, R., et al. 2009, *A&A*, 506, 1183
- Busquet, G., Palau, A., Estalella, R. et al. 2010, *A&A*, 517, L6
- Campbell, M. F., Sridharan, T.K., Beuther, H. et al. 2008, *ApJ*, 673, 954
- Carral, P., Kurtz, S., Rodriguez, L.F. et al. 1999, *RMxAA*, 35, 97
- Caselli, P., Walmsley C.M., Zucconi, A. et al. 2002, *ApJ*, 565, 344
- Flower, D. R., Pineau Des Forêts, G., & Walmsley, C. M. 2006, 456, 215
- Fontani, F., Caselli, P., Zhang, Q. et al. 2012, arXiv:1203.3412
- Fontani, F., Zhang, Q., Caselli, P., Bourke, T.L. 2009, *A&A*, 499, 233
- Fontani, F., Caselli, P., Bourke, T.L., Cesaroni, R., Brand, J. 2008, *A&A*, 477, L45
- Foster, J.B., Rosolowsky, E.W., Kauffmann, J., et al. 2009, *ApJ*, 696, 298
- Friesen, R.K., Di Francesco, J., Shirley, Y.L., Myers, P.C. 2009, *ApJ*, 697, 1457
- Fuente, A., Martin-Pintado, J., Cernicharo, J., Bachiller, R. 1993, *A&A*, 276, 473
- Gerin, M., Kaźmierczak, M., Jastrzebska, M. et al. 2011, *A&A*, 525, A116
- Gerin, M., Goicoechea, J.R., Pety, J., Hily-Blant, P. 2009, *A&A*, 494, 977
- Hennebelle, P.; Commerçon, B.; Joos, M. et al. 2011, *A&A*, 528, 72
- Hill, T., Thompson, M.A., Burton, M.G. 2006, *MNRAS*, 368, 1223
- Ho, P.T.P. & Townes, C.H. 1983, *ARA&A*, 21, 239
- Kirk, H., Johnstone, D., & Tafalla, M. 2007, *ApJ*, 668, 1042
- Kramer, C., Alves, J., Lada, C., et al. 1998, *A&A*, 329, L33
- Krumholz, M.R., Klein, R.I., McKee, C.F. 2011, *ApJ*, 740, 74
- Krumholz, M. & McKee, C.F. 2008, *Nature*, 451, 1082
- Kumar, M.S.N., Bachiller, R., & Davis, C. J. 2002, *ApJ*, 576, 313
- Lee, H.-G., Koo, B.-C., Park, Y.-S., Ho, P. T. P. 2002, *JKAS*, 35, 105
- Linsky, J. L., et al. 2006, *ApJ*, 647, 1106
- Longmore, S. N., Burton, M. G., Barnes, P. J. et al. 2007, *MNRAS*, 379, 535
- Lucas, R. & Liszt, H.S. 2000, *A&A*, 358, 1069
- MacLaren, I., Richardson, K.M. & Wolfendale, A.W. 1988, *ApJ*, 333, 821
- Miralles, M.P., Rodriguez, L.F., Tapia, M., et al. 1994, *A&A*, 282, 547
- Molinari, S., Brand, J., Cesaroni, R., & Palla, F. 2000, *A&A*, 355, 617
- Mul, P.M. & McGowan, J.W. 1980, *ApJ*, 237, 749
- Müller, H. S. P., Thorwirth, S., Roth, D. A., & Winnewisser, G. 2001, *A&A*, 370, L49
- Padovani, M., Walmsley, C.M., Tafalla, M., Galli, D., Müller, H.S.P. 2009, *A&A*, 505, 1199
- Palau, A., Estalella, R., Girart, J.M., et al. 2007a, *A&A*, 465, 219
- Palau, Aina, Estalella, R., Ho, P.T.P., Beuther, H., Beltrán, M.T. 2007b, *A&A*, 474, 911
- Palau, Aina, Sánchez-Monge, Á., Busquet, G., et al. 2010, *A&A*, 510, A5
- Panagia, N. 1973, *ApJ*, 78, 929
- Park, Y.-S. 2001, *A&A*, 376, 348
- Peeters, E., Hony, S., Van Kerckhoven, C. et al. 2002, *A&A*, 390, 1089
- Pety, J., Teyssier, D., Fossé, D. et al. 2005, *A&A*, 435, 885
- Pillai, T., Kauffmann, J., Wyrowski, F. et al. 2011, *A&A*, 530, 118
- Pillai, T., Wyrowski, F., Hatchell, Gibb, J.A.G., Thompson, M.A. 2007, *A&A*, 467, 207
- Purcell, C. R., Minier, V., Longmore, S. N. et al. 2009, *A&A*, 504, 139
- Roueff, E., Lis, D.C., van der Tak, F.F.S., Gerin, M., Goldsmith, P.F. 2005, *A&A*, 438, 585
- Rygl, K.L.J., Brunthaler, A., Sanna, A. et al. 2011, arXiv1111.7023
- Sakai, N., Saruwatari, O., Sakai, T., Takano, S., Yamamoto, S. 2010, *A&A*, 512, 31
- Sridharan, T. K., Beuther, H., Schilke, P., Menten, K. M., Wyrowski, F. 2002, *ApJ*, 566, 931
- Stutzki, J. & Winnewisser, G. 1985, *A&A*, 144, 13
- Tafalla, M., Myers, P.C., Caselli, P., & Walmsley, C.M. 2004, *A&A*, 416, 191
- Torrelles, J.M., Verdes-Montenegro, L., Ho, P.T.P., Rodriguez, L.F., Canto, J. 1993, *ApJ*, 410, 202
- Walsh, A. J., Myers, P. C., Di Francesco, J., et al., 2007, *ApJ*, 655, 958
- Zhang, Q., Hunter, T.R., Brand, J. et al. 2005, *ApJ*, 625, 864
- Zhang, Q., Hunter, T.R., Sridharan, T.K., Ho, P.T.P. 2002, *ApJ*, 566, 982

APPENDIX A: ANALYSIS FOR THE CASE OF DIFFERENT T_{ex} FOR THE MAIN AND THE INNER SATELLITE LINES OF NH_3 (1, 1)

Let us assume that the linewidth of the magnetic hyperfine components of the NH_3 (1, 1) inversion transition is large

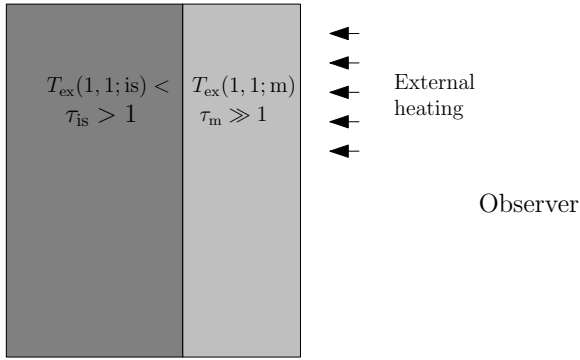


Figure A-1. Geometry of MMA

enough to make them unresolved, so that only the five electric hyperfine lines, i.e. one main line (“m”), two inner satellites (“is”), and two outer satellites (“os”), are resolved. Assuming that the excitation temperature is $T_{\text{ex}} \gg T_{\text{bg}}$, the ratio of intensities of the main line to the inner satellite line is

$$\frac{T_{\text{MB}}(1, 1; \text{is})}{T_{\text{MB}}(1, 1; \text{m})} = \frac{T_{\text{ex}}(1, 1; \text{is})(1 - e^{-\tau_{\text{is}}})}{T_{\text{ex}}(1, 1; \text{m})(1 - e^{-\tau_{\text{m}}})}. \quad (\text{A-1})$$

The usual assumption is that we are observing a homogeneous isothermal region, so that both excitation temperatures, $T_{\text{ex}}(1, 1; \text{is})$ and $T_{\text{ex}}(1, 1; \text{m})$, are equal, and that $\tau_{\text{is}} = 0.28 \tau_{\text{m}}$. In this case,

$$0.28 \leq \frac{T_{\text{MB}}(1, 1; \text{is})}{T_{\text{MB}}(1, 1; \text{m})} \leq 1. \quad (\text{A-2})$$

The lower limit corresponds to the optically thin case, while the upper limit is the optically thick case.

In Sect. 3.2.2 we have shown $\text{NH}_3(1, 1)$ spectra for each of the 3 mm continuum clumps. For the case of MMA, the intensity ratio of the inner satellites and the main line is 0.23 ± 0.05 , lower than the optically thin limit, 0.28.

The assumption that the observed ratio is close to 0.28, and that the emission in MMA is optically thin, leads to inconsistent results. For an optical depth of the main line of $\tau_{\text{m}} < 0.1$, we obtain that $T_{\text{ex}} > 230$ K, which is much higher than the kinetic temperature estimated from the intensities ratio $T_{\text{MB}}(2, 2)/T_{\text{MB}}(1, 1)$ (see text), $T_{\text{k}} = 22$ K. This result is improbable, since we expect the excitation temperature to be, in general, lower than the kinetic temperature.

The intensity of the $(1, 1; \text{m})$ is close to the kinetic temperature, indicating that the optical depth of the main line is probably $\tau_{\text{m}} \gg 1$. The optical depth of the satellite, however, can be lower, so that both lines are tracing the emission of different layers of the region observed: the main line, the outer layer facing the observer; and the satellite line, a deeper layer of material (see Fig. A-1). The easiest explanation of the anomalous ratio $T_{\text{MB}}(1, 1; \text{is})/T_{\text{MB}}(1, 1; \text{m})$ is to assume that the region is not isothermal, and that the two layers at different physical depths, have different temperatures. So, the two excitation temperatures, $T_{\text{ex}}(1, 1; \text{is})$ and $T_{\text{ex}}(1, 1; \text{m})$, are not equal. Thus,

$$\frac{T_{\text{ex}}(1, 1; \text{is})}{T_{\text{ex}}(1, 1; \text{m})} \frac{1 - e^{-\tau_{\text{is}}}}{1 - e^{-\tau_{\text{m}}}} = \frac{T_{\text{MB}}(1, 1; \text{is})}{T_{\text{MB}}(1, 1; \text{m})} = 0.23. \quad (\text{A-3})$$

Assuming that $T_{\text{ex}}(1, 1; \text{m})$ is lower than T_{k} ,

$$T_{\text{MB}}(1, 1; \text{m}) \leq T_{\text{k}}(1 - e^{-\tau_{\text{m}}}), \quad (\text{A-4})$$

giving that the optical depth of the main line must be $\tau_{\text{m}} \geq 3.1$. Thus, taking into account that $\tau_{\text{is}} = 0.28 \tau_{\text{m}}$, we obtain

$$0.61 \leq \frac{1 - e^{-\tau_{\text{is}}}}{1 - e^{-\tau_{\text{m}}}} \leq 1, \quad (\text{A-5})$$

resulting in

$$0.23 \leq \frac{T_{\text{ex}}(1, 1; \text{is})}{T_{\text{ex}}(1, 1; \text{m})} \leq 0.38. \quad (\text{A-6})$$

The result is that the deeper layer traced by the satellite line is colder than the outer layer traced by the main line. If we assume that the kinetic temperature of MMA, obtained from the ratio $T_{\text{MB}}(2, 2)/T_{\text{MB}}(1, 1)$, is tracing the outer layer, the outer layer temperature is 22 K, while the inner layer temperature is between 5 K and 8 K. The higher temperature of the outer layer is indicative of external heating, as discussed in the text.